

Radio Science

RESEARCH ARTICLE

10.1029/2018RS006773

Key Points:

- Implementation of a low cost, software-defined HF radar for ionospheric research is explained
- Open-source software and commercial-off-the-shelf products are used
- The system allows comprehensive analysis of events such as sporadic *E* and spread *F*

Correspondence to:

S. M. Bostan,
salih_bostan@yahoo.com

Citation:

Bostan, S. M., Urbina, J., Mathews, J. D., Bilén, S. G., & Breakall, J. K. (2019). An HF software-defined radar to study the ionosphere. *Radio Science*, 54, 839–849. <https://doi.org/10.1029/2018RS006773>

Received 26 NOV 2018

Accepted 13 AUG 2019

Accepted article online 21 AUG 2019

Published online 10 SEP 2019

An HF Software-Defined Radar to Study the Ionosphere

Salih Mehmed Bostan¹ , Julio V. Urbina¹, John D. Mathews¹, Sven G. Bilén¹ , and James K. Breakall¹

¹Department of Electrical Engineering, The Pennsylvania State University, State College, PA, USA

Abstract In this paper, a novel design and implementation of a software-defined high-frequency ionospheric radar, the Penn State Ionospheric Radar Imager (PIRI), is described. Furthermore, preliminary results produced by the system (located at 40.71° N, 77.97° W) are presented. PIRI is designed to be a modest and low-cost radar system, which is composed mostly of commercial-off-the-shelf products and utilizing open-source software to perform pulse generation, pulse coding, downconversion, data acquisition, and signal processing. It is designed to be mobile, as it can easily be deployed at temporary locations to study local ionospheric disturbances. For the results presented herein, the radar operating frequency was 5.125 MHz. However, as the system is software defined and short active receive antennas are used, only the transmit antenna needs to be changed to operate over the entire high-frequency (HF) band. The two orthogonal receive antennas enable both linear and circular polarization measurements. Peak transmit power of the system is 500 W. PIRI is designed to be a modest and cost-effective alternative to the current standard HF ionospheric sounding systems and can be readily replicated.

1. Introduction

Remote sensing of the ionosphere using ionosondes and radars has played a crucial role in space research for over 80 years (Reinisch et al., 2009; Woodman, 1991). Ionospheric sounders have been used to observe solar cycle, diurnal, and seasonal variations of the ionosphere and to investigate how solar activity impacts the formation of the ionosphere and related phenomena such as sporadic *E* (Mathews, 1998) and spread *F*. In 1925, Appleton and Barnett (Appleton & Barnett, 1925) observed local diurnal variation of transmitted signals using a method that varied the frequency of the transmitter after each pulse. In 1926, Breit and Tuve (1926) used pulses at a fixed frequency instead of chirping the pulses to determine the height of the ionized layer, which proved the existence of echoes from the upper regions of the Earth's atmosphere. These two different methods—frequency chirping and pulsing—were developed independently and continue to be used in both ionosondes and radar sensors (Bibl, 1998). Cost is an important requirement for ionospheric sounders, since a dense network of systems is required to image the global formation of the ionosphere (Bibl & Reinisch, 1978). It was not until the 1970s that digital integrated circuits came onto the market at prices that allowed the design and construction of relatively low-cost digital ionosondes, which are also known as digisondes (Bibl & Reinisch, 1978). Since then, different digital ionosonde and high-frequency (HF) ionospheric radar implementations have been reported (Chen et al., 2009; Davies & Cannon, 1994; Greenwald et al., 1995; Grubb et al., 2008; Hackett, 2013; Huang et al., 2013; MacDougall et al., 1995; Reinisch et al., 2009; Zuccheretti et al., 2003).

Progress in the development of digital integrated circuits has enabled new state-of-the-art radio communication technologies that are capable of directly sampling radio frequency (RF) signals, processing the data in the digital domain, and being reconfigurable by means of software. In the context of radar systems, this technology is referred to as software-defined radar (SDR), a term derived from software-defined radio. SDR systems can be easily configured in software, giving them many advantages including the possibility of creating a multipurpose radar, ease of implementing advanced signal processing techniques, low cost, reduced development time, and the capability of reusing the same hardware (Debatty, 2010). In recent years, SDRs have gained popularity in ionospheric research, and different systems have been introduced. An experimental software-defined radio-based receiver utilizing ionospheric sounders is reported by Vierinen (2013). A continuous wave HF beacon network has been deployed at various locations of the Peruvian sector to study equatorial spread *F* (Hysell et al., 2016) and have also been used for space weather forecasting (Hysell et al., 2018). In order to provide improved ionospheric sounding capabilities to the scientific community, we have

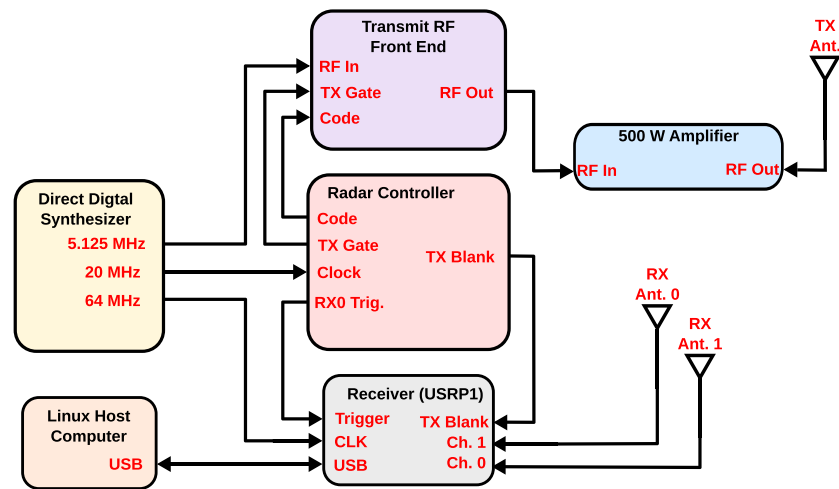


Figure 1. Block diagram of Penn State Ionospheric Radar Imager. RF = radio frequency.

developed an SDR system, described herein, with the main objectives of making it more cost-effective, easily implementable, and more capable especially for studying ionospheric interactions (Seal, 2014; Sorbello et al., 2015; Tuysuz et al., 2013).

A dense network of ionosondes around the world is well established. This network provides useful information about ionospheric conditions as well as plasma instabilities such as spread *F* and layered structures such as sporadic *E*. However, ionosondes are not practical for observation of transient perturbations occurring in the ionosphere, as they typically sweep over a wide range of frequencies. Even though ionosondes can operate in radar mode, their fixed frequency sounding capabilities are limited compared to a dedicated radar (Kamil & Adel, 2014; MacDougall & Li, 2001). On the other hand, conventional HF backscatter radars are designed to operate at a fixed frequency, yet their design does not have the freedom of selection of different frequencies as that capability requires modification of frequency-dependent hardware. An exception for this case is the VIPIR system, which is designed to operate in both radar and ionosonde modes and is the closest solution to an SDR system (Grubb et al., 2008; Reyes, 2017).

In this paper, the design and implementation of a software-defined HF radar system called the Penn State Ionospheric Radar Imager (Piri) is described. Being completely software defined, the main advantage of Piri over conventional ionospheric radars is that it covers the entire HF band without any need to make changes in hardware, other than the transmit antenna (unless a wideband antenna is available). The system was developed largely using commercial-off-the-shelf hardware and open-source software. As such, it is a cost-effective alternative to current ionospheric sounders.

The remainder of this paper is as follows. In section 2, an overview of the system describing its main hardware and software components is given. Observational results from selected data sets to demonstrate the capabilities of the radar system are presented in section 3, and, finally, concluding remarks are provided in section 4.

2. System Description

Piri is a versatile, low-cost SDR designed to be operated at HF for use in ionospheric research. The system largely utilizes commercial-off-the-shelf hardware and open-source software to provide signal generation, signal processing, downconversion, data acquisition, and transmit–receive control for ionospheric sounding. Current deployment of Piri is at Rock Springs, PA (40.71° N, 77.97° W), near the Penn State, University Park campus. Figure 1 shows the block diagram of Piri. The major components of the radar system are listed in Table 1. A 500-W broadband solid-state amplifier from Amplifier Research (Amplifier Research, 2019) is used to amplify the transmit pulse. The transmit front end consists of a custom made, that is, noncommercial-off-the-shelf barker coding circuitry. Core components of the Piri system are described in the following subsections.

Table 1
Main Components of PIRI

Component	Description
Transmit antenna	Inverted V-halfwave dipole
Transmit RF front-end	RF gating: mini circuits ZYSW-2-50DR
Transmit RF front-end	RF amplifier: mini circuits ZFL-500LN
Receive antenna	DX-Engineering ARAH3-1P
Power amplifier	Amplifier research 500A100A (500 W)
Data acquisition software	GnuRadar
Receiver hardware	USRP1
Radar controller hardware	Opal Kelly XEM3001v2
Radar controller software	Bit Pattern Generator
Direct digital synthesizer	Novatech DDS9m

Note. PIRI = Penn State Ionospheric Radar Imager; RF = radio frequency.

2.1. Antenna Setup

2.1.1. Transmit Antenna

A common antenna type used by the amateur radio community, namely, the inverted-V dipole, is used for PIRI. As given in Figure 2 (left), the inverted-V dipole has the shape of an upside down letter “V” as the center of the dipole is mounted on a 40-ft (12-m) tower and both of its legs are bent down toward the ground. Wavelengths at HF frequencies are relatively long, and in this frequency range antennas can occupy large areas. Even though the peak gain of the inverted-V antenna is slightly lower than a horizontal dipole, they are useful for HAM radio communication, especially in urban areas, since they do not occupy large horizontal area. Therefore, instead of erecting a dedicated antenna tower for PIRI, the location of PIRI was chosen to be near an existing HAM radio tower, and an inverted-V dipole antenna was mounted on that tower located near Rock Springs, PA.

Feko electromagnetic modeling software was used to analyze the antenna’s characteristics. In the antenna model, ground surface was included, and the radiation pattern is given in Figure 2, right (Feko, 2014). The center frequency of the antenna is 5.125 MHz, and the voltage standing-wave ratio of the antenna is less than 1.2 over a 50-kHz bandwidth. Half-power beamwidth of the antenna in the elevation plane is 83.5° at $\phi = 0^\circ$, 109.8° at $\phi = 45^\circ$, and 128.2° at $\phi = 90^\circ$. The transmitting antenna beam points vertically upward at zenith, and it is horizontally polarized.

The material used to construct the antenna is stranded aerial copper wire known as “wire rope” and is 14 American wire gauge in diameter. These types of thin wires are widely used in the HAM radio community due to their flexibility and resistance to oxidation. Wire rope can also be tied to the insulators to make

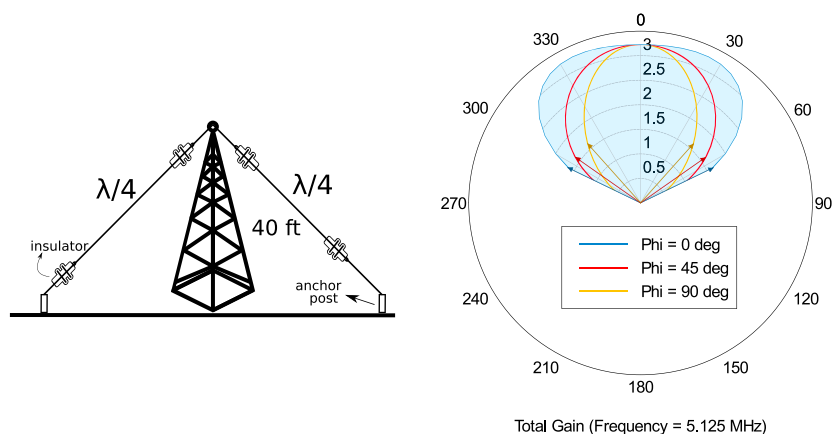


Figure 2. Physical sketch of the transmission antenna (Left) and corresponding radiation pattern in the plane of the polarization (Right).

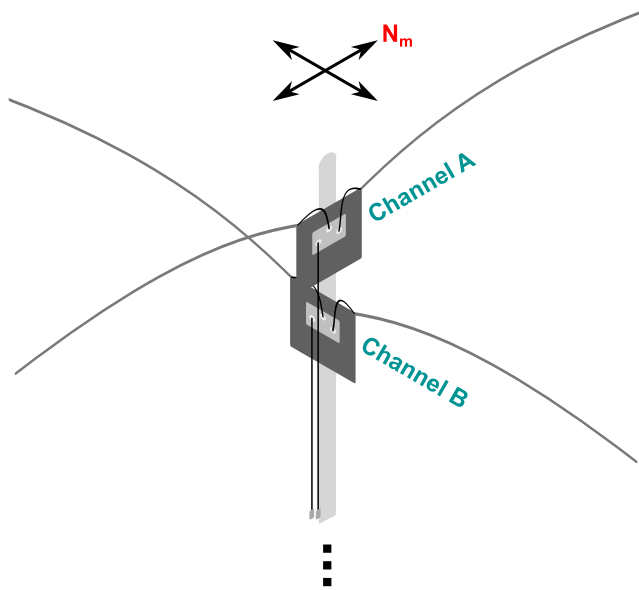


Figure 3. Physical sketch of the receiving antennas with N_m denoting magnetic North (Hackett, 2013).

adjustments to keep the antenna at the same resonating frequency because the voltage standing-wave ratio performance tends to degrade over time.

2.1.2. Receive Antenna

PIRI uses two wideband DX Engineering ARAH3-1P active antennas (DX-Engineering, 2018). ARAH3-1P is a 102-in. (2.6-m) dual-whip antenna operating between 100 kHz and 30 MHz, with a third-order intercept of approximately +30 dBm. They provide weak signal sensitivity, and due to their small size with respect to full size antennas, they are easy to mount and install. Even though it is designed for the amateur radio community, it provides good sensitivity over a wide frequency range and is useful for PIRI, as it is designed to cover the entire HF band.

The two active antennas are placed orthogonally with respect to each other so that they can be used in both linear and circular polarization modes, which allows ordinary and extraordinary mode analysis of the signals. As illustrated in Figure 3, one of the antennas is aligned with the magnetic north, whereas the other one is aligned with magnetic East. HF noise consists of various external sources, such as atmospheric/lightning, solar, galactic, and man-made and therefore exhibits both diurnal and seasonal variations (Giesbrecht, 2008). Depending on these variabilities in the HF noise, preamplification of the active antennas may not be sufficient for signal conditioning, resulting in poor signal-to-noise ratio (SNR). In such cases, additional low noise amplifiers can be added to maximize the overall SNR by reducing the noise figure contribution of the receiver and the front end. We also found that our data are always dominated by nonthermal interference sources such as distant radio transmitters and local power line arcing. The interfering signals raised the noise floor considerably.

efficient for signal conditioning, resulting in poor signal-to-noise ratio (SNR). In such cases, additional low noise amplifiers can be added to maximize the overall SNR by reducing the noise figure contribution of the receiver and the front end. We also found that our data are always dominated by nonthermal interference sources such as distant radio transmitters and local power line arcing. The interfering signals raised the noise floor considerably.

2.2. System Clock

A clock signal is required for synchronizing the operations of an electronic system. As a radar consists of multiple digital hardware components in both receive and transmit segments, coordination of the timing between each component is necessary for its operation. An accurate clock is also important in a pulsed radar in order to preserve the phase information used in the decoding and/or other signal processing processes. There were three considerations for the selection of the correct clock generator for PIRI. First, crystal oscillators are prone to drift due to aging and temperature. Over time, drifting affects the phase alignment in the clock's output resulting in phase jitter. Thus, good phase stability performance over time is important. Second, PIRI has one Universal Software Radio Peripheral 1 (USRP1) receiver (Ettus Research, 2018) to acquire, digitize, and downconvert the returned radar signal and a radar controller, which requires a clock for synchronization between the two. Third, a frequency generator is needed to generate the carrier frequency for the radar pulse, which also must be synchronous with the system. Therefore, the Novatech DDS9m (Novatech, 2018) direct digital synthesizer (DDS) was selected as the system clock for PIRI since it provides stable and synchronous clock signal. In Figure 1, the signal path for each DDS output frequency is shown.

2.3. Radar Controller

The radar controller generates the complex code pulse patterns and interpulse period (IPP) structure providing flexibility to the radar. Furthermore, the radar controller can also provide accurate timing for the user to gate on/off the receiver for protection during transmission and to establish the receive/sampling window. In general, a radar controller should provide the following (Seal et al., 2008):

- high precision timing between transmit and receive segments of the radar system;
- capability for a wide range of complex pulse schemes and IPPs for different radar operation modes; and
- a user-friendly and customizable interface.

PIRI uses a radar controller that provides high precision timing signals for synchronized operation of its subsystems. The waveform of these timing signals is defined by various radar parameters such as IPP, pulse width, baud length, phase code, and receiver range window. The distribution of specific signals throughout the radar system is displayed in Figure 1. The radar controller is based on commercial-off-the-shelf hardware

and open-source software, and the details of the system are described in Seal et al. (2008), Seal (2017), and Hackett (2013).

Briefly, a commercial FPGA board, Opal Kelley XEM3001v2, is used as the core of the radar controller for tasks such as providing stable, high precision, and reconfigurable timing signals. There are 16 TTL-compatible 50-Ω outputs on its front panel. These outputs can be divided into two groups, and each group can be programmed separately for different radar configurations (e.g., allowing control of two radars). The radar controller includes 1-PPS input, which allows the device to be locked to a GPS timing signal. A mini-ITX computer running Linux OS is used for configuring, operating, and monitoring the instrument. The Ethernet port on the computer allows remote operations. An open-source software application called Bit Pattern Generator is used for programming the radar controller. Again, the radar controller determines the transmit/receive properties of the radar via generation of the various digital waveforms needed.

2.4. GnuRadar

As a SDR, most of PIRI's distinctive features lie within software. These features include radar reconfiguration without hardware changes, digitizing the analog input signal, and implementation of signal processing algorithms. Design considerations for PIRI's data acquisition software included the following:

- a routine that is capable of acquiring pulsed radar data continuously without interruption;
- organized data storage of I/Q samples allowing easy implementation of applied signal processing techniques; and
- a user-friendly interface for flexible and reconfigurable radar operation.

The solution addressing these requirements was GnuRadar, an open-source radar software that acquires I/Q data samples utilizing a digital receiver and is designed with the intention of being used for various radar applications (Seal, 2014, 2012). The digital receiver utilizing GnuRadar is the USRP1 board, a member of the USRP device family by Ettus Research, a subsidiary of National Instruments (Ettus Research, 2018). Along with the USRP1 board, one BasicRX daughterboard is used to provide direct access to analog-to-digital converter inputs of the board. USRP devices have been very popular in the scientific and engineering communities and with hobbyists for over a decade. The details of operating GnuRadar software with a USRP1 device are described in Hackett (2013) and Seal (2014). Succinctly, GnuRadar provides program packages for parameter-based radar mode configuration, verification of pulse schemes for synchronous operation, and data acquisition for pulsed radar operation. It should be noted that the USRP1 has discontinued; however, GnuRadar has a custom firmware that is portable to other software-defined radio platforms, and the firmware is available for the community (Seal, 2012).

2.5. Data Storage in HDF5 Format

GnuRadar software uses a popular data format known as Hierarchical Data Format (HDF) for storing the acquired radar data. HDF5 is a format that supports a wide range of data types and is designed to handle high-volume and complex data efficiently (The HDF Group, 1997). Radar operation is expected to be continuous, and the data storage could be very large depending on the total period and complexity of a particular observing session. By default, an open HDF5 file is written to until the system closes the file; however, using large data files is not a reliable means for data collection since a system failure may damage the whole data set. Visual representation of the data format is given in Figure 4. GnuRadar stores the data in 2-GB data files, and each data file consists of a data header and a number of data tables. Each row in the data table corresponds to an IPP, and each column represents all sampled ranges within a given receive window. In Figure 4, each range cell is denoted as R_X^I or R_Y^Q , where I and Q represent in-phase and quadrature components, respectively, saved in the corresponding range cell. At the beginning of a radar operation, the very first header that is generated by the GnuRadar software contains the radar parameters such as IPP, sample rate, and receive window, which are used later in postprocessing algorithms.

2.6. Postprocessing Routines

A number of signal processing routines are applied to the radar data. These routines are as follows:

• DC-offset removal

DC offset occurs in the radar data due to hardware imperfections in the radar system. The complex envelope of a radar signal received by the receiver front-end can be expressed as (excluding clutter)

$$x(t) = s(t) + n(t) \pm DC_{\text{offset}}, \quad (1)$$

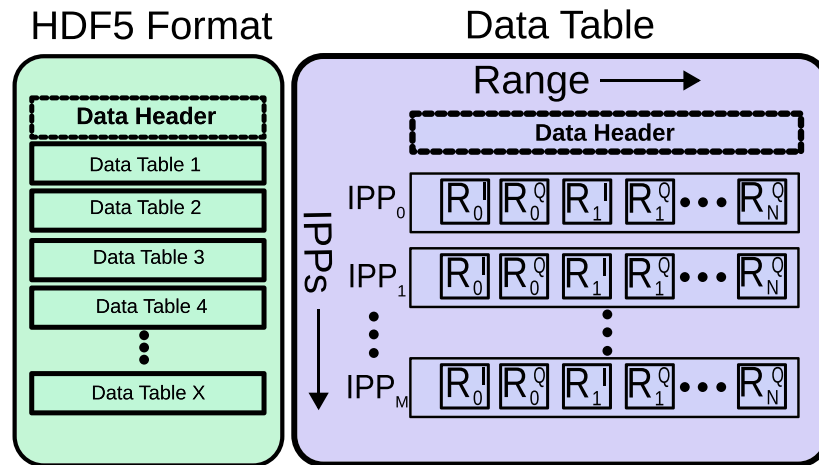


Figure 4. A typical Hierarchical Data Format Version 5 data structure used by GnuRadAr (Seal, 2014).

where $s(t)$ is the target echo, $n(t)$ is the noise, and DC_{offset} is the DC component that may be present due to imperfections in the electronic equipment that is used in the radar system. In digital signal processing, the discrete Fourier transform of a signal $x(t)$ is given by

$$X_k = \sum_{n=0}^{N-1} x_n \cdot e^{-\frac{2\pi i}{N} kn}. \quad (2)$$

Mathematically, the first term of equation (2), x_0 , is the DC component in the Fourier domain. The DC offset in the radar data can be detected by taking the average of in-phase and quadrature samples in the time domain. For the case of a DC offset, it can be removed by subtracting or by adding the offset value from or to each sample.

• **Interference removal**

At the radar's location, man-made electromagnetic interference established the highly dynamic noise floor, which varied by sometimes tens of decibels in a single IPP. The PIRI RF receiver front-end uses wideband (100 kHz to 30 MHz) active antennas that respond to all signals over the entire bandwidth. Wideband interference is removed at baseband by a basic low-pass finite impulse response filter (Lyons, 2011). The passband and the stopband of the filter are determined by the baud length of the radar pulse. In addition to the usually dominant man-made noise, naturally occurring noise such as lightning bursts totally mask the thermal noise at the receiver front-end (Committee, 1983). As a result, even though the target scatterer likely maintains its physical properties over IPP-to-IPP time spans, the observed radar signals often vary randomly and over a large dynamic range from IPP to IPP. Due to this adverse interference/noise environment, our attempts to determine the thermal noise floor and, thus, generate absolute SNR plots failed (Bostan, 2018). Similar to the foundation of Giesbrecht (2008), our extensive analysis revealed that the observed noise does not match with any probability density function and can only be compared locally in time rather than over the observing period of several hours. Hence, the "local" SNR calculations for PIRI data are done by using Hildebrand's very well known approach (Hildebrand & Sekhon, 1974). This approach assumes that the noise is, locally in time, Gaussian. However, this means that absolute SNRs are not available. That is, the SNRs observed from apparently the same ionospheric structure at two somewhat different times are not comparable on an absolute basis.

• **Sidelobe-free decoding**

Similar to other ionospheric radars, PIRI uses a common pulse compression technique, namely, Barker coding, to improve its range resolution and SNR. Matched filtering is the most common method to decode Barker codes; however, the weight function of the matched filter generates sidelobes and, in cases where high and low SNR returns are close to each other, these sidelobes may be distractive (Lehtinen et al., 2004). Efforts to remove these sidelobes were first introduced by Sulzer (1989), and a decoding algorithm that produces zero sidelobes suggested by Lehtinen et al. (2004) is used for the data presented in this paper.

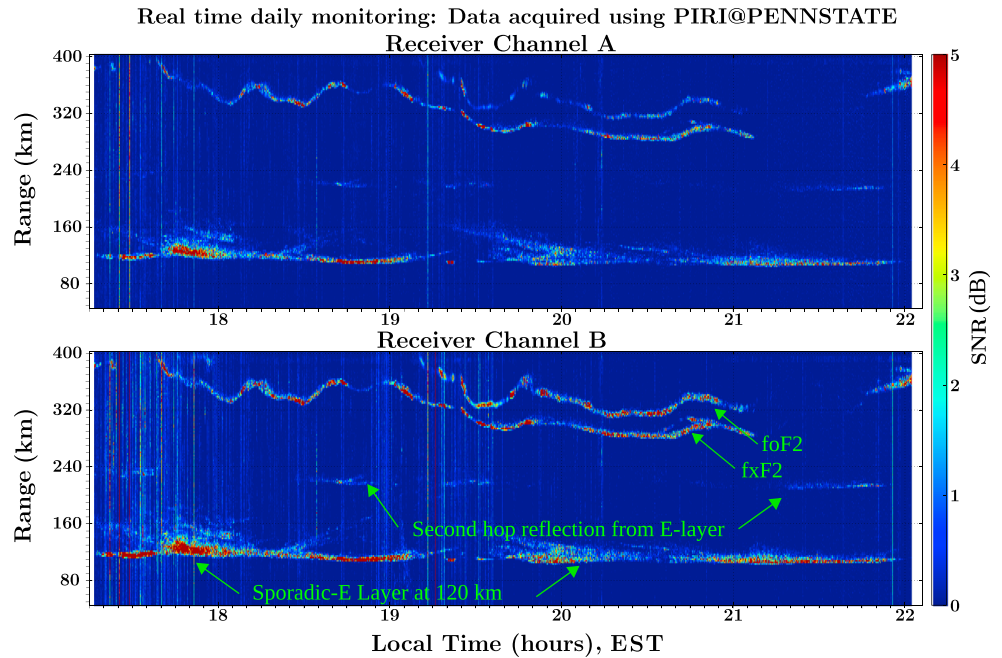


Figure 5. Five-hour-long range-time intensity plot from a sporadic *E* event captured by the Penn State Ionospheric Radar Imager (PIRI) high-frequency radar system (40.71° N, 77.97° W) on 11 August 2016. Channels A and B denote two independent receive channels and the corresponding antennas are placed orthogonal to each other. Range-time intensities are generated by incoherently integrating 200 interpulse periods (1 s) since shorter integration is not feasible for hours-long plots. However, millisecond resolution is available. The radar operation is at a single frequency ($f = 5.125$ MHz), and plots are generated by applying a sidelobe-free decoding filter (Kesaraju et al., 2017; Lehtinen et al., 2004) to a Barker-13-coded radar pulse. Notice that *E* and *F* region returns are received at the same time. This implies that the *E* region return is from scattering, as the *F* region return is also visible. That is, we infer that the *F* region is illuminated through “holes” in the *E* region, meaning the *E* region structure is comprised of altitude-thin “blobs” of order of a few wavelengths in horizontal extent that scatter, yielding the return we observe but also allow significant energy through the *E* region (in both directions) allowing observation of an unusual *F* region. SNR = signal-to-noise ratio.

The decoding filter that produces zero sidelobe is given as

$$h_d[n] = \mathcal{F}_D^{-1} \left\{ \frac{1}{\mathcal{F}_D \{h_c[n]\}} \right\}, \quad (3)$$

where $h_d[n]$ is the decoding filter and is the inverse of the coding filter, $h_c[n]$, in frequency domain, which is the essence of this technique. Similar implementation of this technique can also be found at Kesaraju et al. (2017), who provide a path to codes that verify this approach. For the case of Barker-13-coded pulses, the SNR performance of the sidelobe-free decoding is 95% with respect to a matched filter.

3. Results

PIRI has been operating at Rock Springs, PA, under FCC license since summer 2016. In this paper, we demonstrate PIRI’s capability as an ionospheric radar through discussion of two sporadic *E* events that were captured by PIRI on 11 August 2016 (Figures 5 and 6) and 14 August 2016 (Figure 7). The entire data set of the August 11 event is 5 hr long starting from 17:00 to 22:00 LT, which includes the presunset and postsunset time periods. The data set from 14 August is 12.5 hr long starting from 2:30 to 15:00 LT. All range-time intensity (RTI) plots are generated after applying the postprocessing routines described in section 2. The radar configuration for PIRI when capturing both data sets are given in Table 2. The IPP of the Barker-13-coded radar pulse is 5 ms. Total pulse width is 195 μ s, and each baud length is 15 μ s, resulting in a range resolution of 2.25 km. A solid-state wideband power amplifier with a peak power of 500 W was used during the observations. In Figure 5, a 5-hr-long RTI plot is given. PIRI has two independent channels, which are denoted

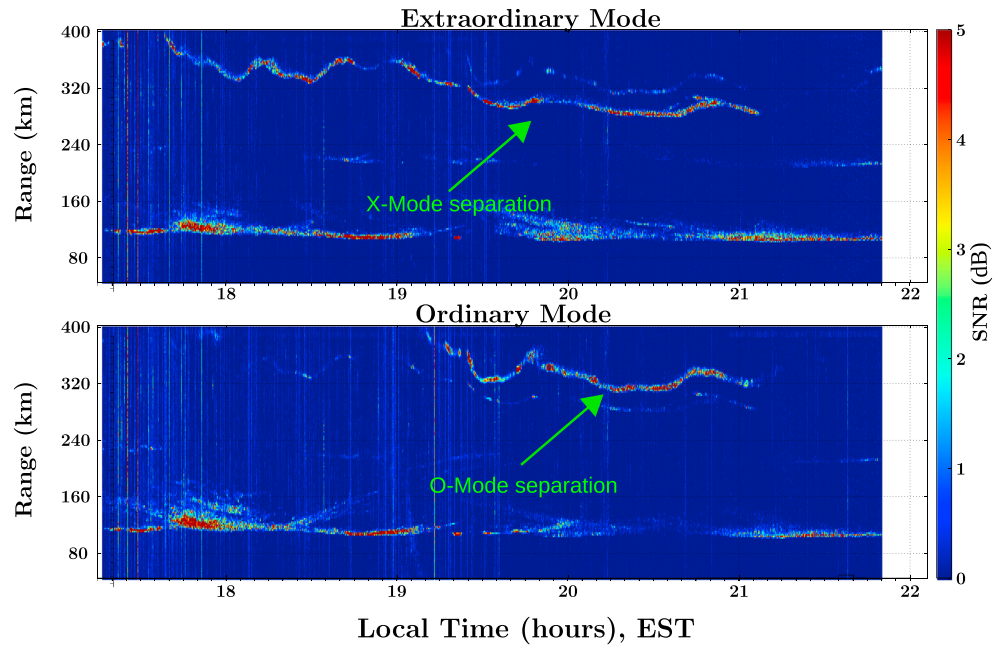


Figure 6. Ordinary (O) and Extraordinary (X) mode range-time intensity plots from the same sporadic *E* event captured by the PIRI HF radar system on Aug 11, 2016. These plots are also generated by the same routines as described in Figure 5. (Top) Receiver channel denotes X-mode and (bottom) receiver channel denotes O-mode.

as Channels A and B. As can be inferred from Figure 5, Channel B has better SNR, which is mostly due to calibration mismatch between the two channels. Range ticks are added for every 10 km, and time ticks are added for every 5 min. Even though the system is capable of sampling the whole IPP range (for 5 ms, up to 750 km), the plotted range was limited to 50 and 400 km since below and above of these altitudes, only noise was present. All features that are captured by the radar system are labeled on the RTI plots. PIRI is located in rural Pennsylvania, and environmental noise is often very strong in the continental United States depending on daytime and nighttime ionospheric conditions. Vertical lines that are present in the figures are due to HF noise saturation in the receiver, and Channel B is more saturated due to slightly higher gain of that channel.

In Figure 5, the sporadic *E* layer lies at a virtual height of 120 km. Sporadic *E* layers are plasma enhancements in the *E* region of the ionosphere that occur in between 90- and 120-km altitude. Formation of sporadic *E* (E_s) can be patchy, which allows partial reflections from higher altitudes (i.e., from ionospheric *F* region)

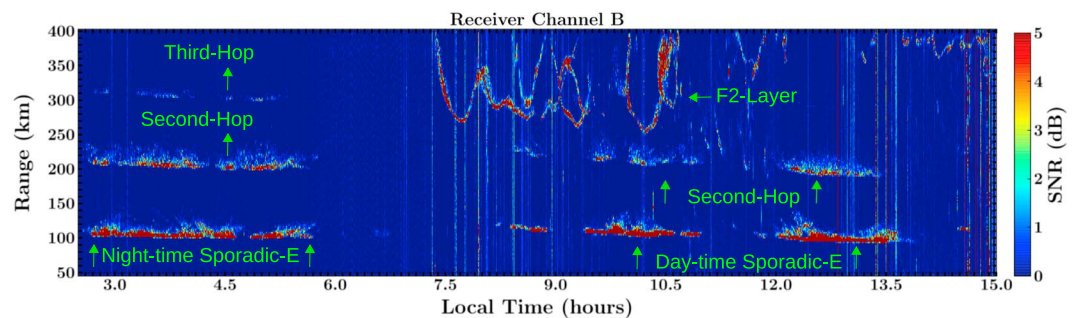


Figure 7. Another range-time intensity plot from a 12.5-hr-long observation with Penn State Ionospheric Radar Imager from from 02:30 to 15:00 LT, on 14 August 2016. Only the single channel is presented for this data set, and the radar parameters are exactly the same as given in Table 2. Nighttime sporadic *E* is 3 hr long, and the scattering is so strong such that third-hop reflection is present. A strong daytime sporadic *E* appears before and after the noon time. Second-hop reflection is also present for the daytime sporadic *E*. Notice that all multihop reflections from both sporadic *E* events have a different structure than their source, which implies that reflections are not just from overhead but also from other Fresnel areas. Another noticeable feature in the figure is that the fixed frequency returns from the *F* layer are very different compared to standard straight *F* layer returns in ionograms, which are generated from multifrequency returns.

Table 2
Radar Configuration for Sporadic E Event on 11 August 2016

Component	Description
Operating frequency	5.125 MHz
IPP	5 ms
Pulse compression	Barker-13
Pulse width	195 μ s
Peak power	500 W

Note. IPP = interpulse period.

or it can be blanketing, which means a total reflection from the layer (Mathews, 1998; Mathews et al., 2001; Mathews & Morton, 1994; Mathews et al., 1993). The E_s presented here has a patchy formation (Malhotra et al., 2008; Gao & Mathews, 2014), and, even in case of double-hop strong E_s layer presence at around 21:00 LT, both foF2 and fxF2 layers (Davies, 1990) are present in the radar data.

PIRI has two crossed-dipole receive antennas, and this configuration allows circular polarization (i.e., ordinary and extraordinary mode) analysis of the data. If V_O and V_X denote the ordinary and extraordinary voltage samples, respectively, then the circular polarization analysis can be performed as follows:

$$V_O = V_A - iV_B, \quad (4)$$

$$V_X = V_A + iV_B, \quad (5)$$

where V_A and V_B denote each in-phase and quadrature voltage sample received by the receiver's Channels A and B, respectively. Ordinary and extraordinary mode plots are given in Figure 6.

The 12.5-hr-long data set from 14 August is given in Figure 7. This data set exhibits major night/day differences. The ionosphere return from the beginning time to 05:45 LT is consistent with blanketing sporadic E in that no F region return is seen and the second and third "hops" from the ionosphere to the ground and back are observed. The vertical structuring of the sporadic E return is real pointing to complex structure in the ionosphere. This structuring may, in part, be due to the micrometeoroid mass flux in the predawn hours (Mathews, 1998). Several processes are also likely coming into play. First, the predawn F region was not visible at any point in this figure. We interpret that as foF2 is below 5 MHz and/or that the F region peak was well above 400 km. This is certainly the case from 10:30 to 15:00 LT. Second, on the 05:45–07:15 interval, the D region with incumbent absorption was coming into play. As some faint sporadic E returns were visible on this interval, this seems likely. Finally, the night-to-day transition may have resulted in significant horizontal gradients (tilts) of the E and F region ionosphere, thus lessening the energy reflected or scattered back to the radar. F layer returns starting from 07:00 LT show clearly a highly perturbed F region. The two F region returns over 07:30 and 09:30 LT interval to be from the approximately overhead ionosphere and from a somewhat more distant tilt of the 5-MHz plasma frequency ionosphere. This seems particularly evident from the two V-shaped returns with the second of these overlapped by an inverted-V return. These results supply considerable context to the very narrow-beam incoherent scatter radar results.

4. Conclusion

Design and implementation of a low-power and low-cost software-defined HF radar are presented. The radar system is largely composed of low-cost commercial-off-the-shelf components, and the system can be adapted for use over the entire HF frequency range by means of software without the need for application-specific integrated circuits. This feature allows easy reconfiguration of the radar system by reusing the same components, with the only exception being the transmitting antenna, unless a wideband antenna is used.

Ionosondes form a dense network around the world since they are used for daily monitoring of ionospheric conditions, and most of the ionospheric research that requires statistical analysis, such as determining the occurrence of spread F and sporadic E , depend on ionosonde data. Even though ionosondes can provide plasma density versus altitude information, due to their operational nature, they cannot provide detailed information of transient events at fixed frequencies, and conventional radar systems are not widely available,

as they are expensive to deploy and maintain. However, ionospheric phenomena are very dynamic and a comprehensive analysis of an event requires short term, that is, pulse-to-pulse analysis. For instance, as observed in resolved and unresolved spread F events detected by ionosondes, radar observations can reveal the actual type of the event (From & Meehan, 1988; Mathews et al., 2001). The radar system presented in here has better time resolution than ionosondes, is highly customizable, and it can be used to resolve the fine details of ionospheric features, as well as providing long-term ionospheric measurements at fixed frequencies.

Acknowledgments

This work has been partially supported under NSF Grant AGS 12-41407 to The Pennsylvania State University and AO/SRI International. The data set for this paper is available online (through <https://doi.org/10.26208/t2ve-bs23>), and for details, please contact Salih Mehmed Bostan (at smbostan@protonmail.com).

References

- Amplifier Research (2019). Ar500a100a. <https://www.arworld.us/> (Accessed March 11, 2019).
- Appleton, E. V., & Barnett, M. (1925). Local reflection of wireless waves from the upper atmosphere. *Nature*, *115*(2888), 333.
- Bibl, K. (1998). Evolution of the ionosonde. *Annali Di Geofisica*, *41*(5-6), 667–680. <https://doi.org/10.4401/ag-3810>
- Bibl, K., & Reinisch, B. W. (1978). The universal digital ionosonde. *Radio Science*, *13*(3), 519–530. <https://doi.org/10.1029/rs013i003p00519>
- Bostan, S. M. (2018). The discovery of novel ionospheric phenomenon using a software-defined high frequency radar (Doctoral dissertation), Electrical Engineering, The Pennsylvania State University, US.
- Breit, G., & Tuve, M. A. (1926). A test of the existence of the conducting layer. *Physical Review*, *28*(3), 554. <https://doi.org/10.1103/physrev.28.554>
- Chen, G., Zhao, Z., Zhu, G., & Shi, S.-Z. (2009). The Wuhan ionospheric sounding systems. *IEEE Geoscience and Remote Sensing Letters*, *6*(4), 748. <https://doi.org/10.1109/lgrs.2009.2024439>
- Committee, I. R. C. (1983). *Characteristics and applications of atmospheric radio noise data* (No. 2, Vol. 322). Geneva: International Telecommunication Union, International Radio Consultative Committee.
- DX-Engineering (2018). ARAH3-1P manual. <https://static.dxengineering.com/global/images/instructions/dxe-arah3-1p.pdf>, Accessed: May, 2018.
- Davies, K. (1990). *Ionospheric radio* (No. 31). London: IET.
- Davies, N. C., & Cannon, P. S. (1994). DAMSON-A system to measure multipath dispersion, Doppler spread and shift on multi-mechanism communications channels. In *Agard conference proceedings agard CP* (pp. 36–36). Malvern.
- Debatty, T. (2010). Software-defined radar: A state of the art, *2010 2nd international workshop on Cognitive information processing (CIP)* (pp. 253–257). Elba, Italy: IEEE. <https://doi.org/10.1109/cip.2010.5604241>
- Ettus Research (2018). Universal software radio peripheral. <https://www.ettus.com/> Accessed April 19, 2018.
- Feko, E. (2014). Simulation software. Version.
- From, W., & Meehan, D. (1988). Mid-latitude spread-F structure. *Journal of Atmospheric and Terrestrial Physics*, *50*(7), 629–638. [https://doi.org/10.1016/0021-9169\(88\)90061-x](https://doi.org/10.1016/0021-9169(88)90061-x)
- Gao, B., & Mathews, J. (2014). High-altitude meteors and meteoroid fragmentation observed at the Jicamarca Radio Observatory. *Monthly Notices of the Royal Astronomical Society*, *446*(4), 3404–3415. <https://doi.org/10.1093/mnras/stu2176>
- Giesbrecht, J. E. (2008). Aspects of HF communications: HF noise and signal features (doctoral dissertation), Electrical Engineering, The University of Adelaide.
- Greenwald, R., Baker, K., Dudeney, J., Pinnock, M., Jones, T., Thomas, E., et al. (1995). Darn/Superdarn. *Space Science Reviews*, *71*(1-4), 761–796. <https://doi.org/10.1007/bf00751350>
- Grubb, R. N., Livingston, R., & Bullett, T. W. (2008). A new general purpose high performance HF radar. XXIX URSI General Assembly.
- Hackett, A. (2013). On the development of modern ionospheric sensors using software-defined radio techniques (Master's thesis), Electrical Engineering, Pennsylvania State University, USA.
- Hildebrand, P. H., & Sekhon, R. (1974). Objective determination of the noise level in doppler spectra. *Journal of Applied Meteorology*, *13*(7), 808–811. [https://doi.org/10.1175/1520-0450\(1974\)013h0808:odotnli2.0.co;2](https://doi.org/10.1175/1520-0450(1974)013h0808:odotnli2.0.co;2)
- Huang, S., Zhao, Z., Yang, G., Chen, G., Li, T., Li, N., & Yang, J. (2013). A new design of low-power portable digital ionosonde. *Advances in Space Research*, *51*(3), 388–394. <https://doi.org/10.1016/j.asr.2012.09.005>
- Hysell, D., Baumgarten, Y., Milla, M., Valdez, A., & Kuyeng, K. (2018). Ionospheric specification and space weather forecasting with an HF beacon network in the peruvian sector. *Journal of Geophysical Research: Space Physics*, *123*, 6851–6864. <https://doi.org/10.1029/2018JA025648>
- Hysell, D., Milla, M., & Vierinen, J. (2016). A multistatic HF beacon network for ionospheric specification in the Peruvian sector. *Radio Science*, *51*, 392–401. <https://doi.org/10.1002/2016RS005951>
- Kamil, Y., & Adel, A. (2014). Meteor induced layers in 2013 observed by ionosonde with high cadence. In *General assembly and scientific symposium (ursi gass), 2014 xxxviii ursi* (pp. 1–4). Beijing, China: IEEE. <https://doi.org/10.1109/ursigass.2014.6929862>
- Kesaraju, S., Mathews, J., Milla, M., & Vierinen, J. (2017). Range-Doppler mapping of space-based targets using the JRO 50 MHz radar. *Earth, Moon, and Planets*, *120*(3), 169–188. <https://doi.org/10.1007/s11038-017-9510-0>
- Lehtinen, M., Damtie, B., & Nygrén, T. (2004). Optimal binary phase codes and sidelobe-free decoding filters with application to incoherent scatter radar. *Annales Geophysicae*, *22*, 1623–1632. <https://doi.org/10.5194/angeo-22-1623-2004>
- Lyons, R. G. (2011). *Understanding digital signal processing* (3rd ed.). Upper Saddle River, NJ: Pearson Education India.
- MacDougall, J., Grant, I., & Shen, X. (1995). The Canadian advanced digital ionosonde: Design and results, URSI INAG Ionospheric Station Inf. Bulletin, UAG-104. [https://doi.org/10.1016/s1364-6826\(00\)00143-7](https://doi.org/10.1016/s1364-6826(00)00143-7)
- MacDougall, J., & Li, X. (2001). Meteor observations with a modern digital ionosonde. *Journal of Atmospheric and Solar-Terrestrial Physics*, *63*(2-3), 135–141.
- Malhotra, A., Mathews, J. D., & Urbina, J. (2008). Effect of meteor ionization on Sporadic-E observed at Jicamarca. *Geophysical Research Letters*, *35*, L15106. <https://doi.org/10.1029/2008gl034661>
- Mathews, J. (1998). Sporadic E: Current views and recent progress. *Journal of Atmospheric and Solar-Terrestrial Physics*, *60*(4), 413–435.
- Mathews, J., Gonzalez, S., Sulzer, M., Zhou, Q.-H., Urbina, J., Kudeki, E., & Franke, S. (2001). Kilometer-scale layered structures inside Spread-F. *Geophysical Research Letters*, *28*(22), 4167–4170. <https://doi.org/10.1029/2001gl013077>
- Mathews, J., Machuga, D., & Zhou, Q. (2001). Evidence for electrodynamic linkages between Spread-F, ion rain, the intermediate layer, and sporadic E: Results from observations and simulations. *Journal of Atmospheric and Solar-Terrestrial Physics*, *63*(14), 1529–1543. [https://doi.org/10.1016/s1364-6826\(01\)00034-7](https://doi.org/10.1016/s1364-6826(01)00034-7)

- Mathews, J., & Morton, Y. (1994). Radar measurements of dynamics and layering processes in the 80–150 km region at Arecibo. *Advances in Space Research*, 14(9), 153–160. [https://doi.org/10.1016/0273-1177\(94\)90128-7](https://doi.org/10.1016/0273-1177(94)90128-7)
- Mathews, J., Morton, Y., & Zhou, Q. (1993). Observations of ion layer motions during the AIDA campaign. *Journal of Atmospheric and Terrestrial Physics*, 55(3), 447–457. [https://doi.org/10.1016/0021-9169\(93\)90080-i](https://doi.org/10.1016/0021-9169(93)90080-i)
- Novatech (2018). Dds9m Board Manual. http://www.novatechsales.com/PDF_files/dds9mdds_lr.pdf
- Reinisch, B. W., Galkin, I. A., Khmyrov, G., Kozlov, A., Bibl, K., Lisysyan, I., et al. (2009). New digisonde for research and monitoring applications. *Radio Science*, 44, RS0A24. <https://doi.org/10.1029/2008rs004115>
- Reyes, P. M. (2017). Study of waves observed in the equatorial ionospheric valley region using Jicamarca ISR and VIPIR ionosonde (PhD Thesis), University of Illinois at Urbana-Champaign.
- Seal, R. (2012). Gnuradar version: 3.0.0. <https://github.com/rseal/GnuRadar>, Latest version: Aug 22, 2012.
- Seal, R. (2014). Software defined radar for VHF meteor research at the Pennsylvania State University (Master's thesis), Electrical Engineering, Pennsylvania State University.
- Seal, R. (2017). Bit pattern generator software v-2.0. <https://github.com/rseal/BitPatternGenerator> Latest version: February 23, 2017.
- Seal, R., Urbina, J., Sulzer, M. P., Aponte, N., & Gonzalez, S. (2008). Design and implementation of a multi-purpose radar controller using open-source tools. In *Radar conference, 2008. radar'08* (pp. 1–4). Rome, Italy: IEEE. <https://doi.org/10.1109/radar.2008.4720909>
- Sorbello, R., Urbina, J., & Stephens, Z. (2015). First steps toward the implementation of a cognitive radar to study plasma instabilities along the magnetic equator. *Radio Science*, 50, 229–237. <https://doi.org/10.1002/2014rs005583>
- Sulzer, M. P. (1989). Recent incoherent scatter techniques. *Advances in Space Research*, 9(5), 153–162.
- The HDF Group (1997). Hierarchical Data Format, Version 5. <https://www.hdfgroup.org/HDF5/>
- Tuysuz, B., Urbina, J., & Lind, F. (2013). Development of a passive VHF radar system using software-defined radio for equatorial plasma instability studies. *Radio Science*, 48, 416–426. <https://doi.org/10.1002/rds.20047>
- Vierinen, J. (2013). Gnu chirp sounder. http://www.sgo.fi/~j/gnu_chirp_sounder/ accessed April 18, 2018.
- Woodman, R. F. (1991). A general statistical instrument theory of atmospheric and ionospheric radars. *Journal of Geophysical Research*, 96(A5), 7911–7928. <https://doi.org/10.1029/90ja02628>
- Zuccheretti, E., Tutone, G., Sciacca, U., Bianchi, C., & Arokiasamy, B. J. (2003). The new AIS-INGV digital ionosonde. *Annals of Geophysics*, 46, 647–659. <https://doi.org/10.4401/ag-4377>